Journal of Alloys and Compounds 712 (2017) 870–877

Contents lists available at ScienceDirect

Journal of Alloys and Compounds

journal homepage: http://www.elsevier.com/locate/jalcom

Transition metal titanium (Ti) doped $LaFeO_3$ nanoparticles for enhanced optical structural and magnetic properties

C. Sasikala [a], N. Durairaj [b], I. Baskaran [a, **], B. Sathyaseelan [c], M. Henini [e, f], E. Manikandan [d, f, *]

[a] Dept of Physics, Arignar Anna Govt. Arts College, Cheyyar, Tamil Nadu, 604407, India
[b] Centre for Crystal Growth, SAS, VIT University, Vellore, 632014, Tamilnadu, India
[c] Dept of Physics, University College of Engineering Arni (A Constituent College of Anna University Chennai), Arni, 632326, Tamil Nadu, India
[d] Dept of Physics, Thiruvalluvar University, TVUCAS Campus, Thennangur, 604408, Tamil Nadu, India
[e] School of Physics and Astronomy, Nottingham Nanotechnology and Nanoscience Center, University of Nottingham, Nottingham, NG7 2RD, United Kingdom
[f] UNESCO UNISA Africa Chair in Nanosciences & Nanotechnology, College of Graduate Studies, University of South Africa, M Ridge, P.O. Box 392, Pretoria, South Africa

ARTICLE INFO

Article history:
Received 6 March 2017
Received in revised form
11 April 2017
Accepted 13 April 2017
Available online 14 April 2017

Keywords:
Crystallite size
Nanoparticles
Co-precipitation method
Magnetic properties
Coercivity

ABSTRACT

A series of $LaFe_{1-x}Ti_xO_3$ (x = 0.0, 0.2, 0.4, 0.6 and 0.8) nanoparticles have been successfully synthesized by simple co-precipitation technique. The synthesized samples (calcined at 800° C/3hr) were characterised for structural, optical and magnetic properties. Structural phase formation of the crystal shows orthorhombic planes of these samples phases. The average crystallite size (D_c) is decreasing with a dopant and found to be varying between ~ 9 and 25 nm. Tailored surface morphology was analyzed using scanning electron microscope (FESEM) and transmission electron microscopes (TEM) with selected area electron diffraction pattern (SAED) also confirms the evolution of orthorhombic phases. Diffuse reflectance spectra (DRS) are recorded to evaluate the variation of optical band gap (E_g) upon titanium doping into the $LaFeO_3$ system. The obtained results attributed that E_g values are increasing with dopant altering between 2.05 and 2.61 eV. The metal oxide (M - O) stretching vibrations and few functional groups are detected from infrared spectra (IR). The weak ferromagnetic behaviour is observed from hysteresis loop behaviour. Additionally, the large hysteresis loop behaviour induces no saturation up to 15 kO_e in nanoparticles coercivity (H_c) and anisotropy constants (K_1) are eventually decreasing with 'x' values.

1. Introduction

The magnetic nanomaterial is a promising candidate material, due to co-existing states of multiple coupled such as magnetism and superconductivity [1–9]. Lanthanum iron oxide ($LaFeO_3$) is an ABO_3 perovskite oxide having an orthorhombic structure [10–13]. It has attracted attention for distinct applications such as electrode materials for fuel cells, photocatalyst, chemical sensors, non-volatile magnetic memory devices and ultrasensitive magnetic read heads of modern hard disk drives, etc. [14–21].

Recently, $LaFeO_3$ (LFO) has got much attention owing to its multiferroicity [22]. It is a G-type antiferromagnetic material possessing high Neel temperature (T_N) of 480 °C. Also shows a ferroelectric transition at 200 °C [21,22]. Orthoferrites are the weak ferromagnetic materials with interesting magneto-optical properties [23,24]. The magnetic structure is illustrated by two face centred cubic sub-lattices. In this structure, each ferric ion (Fe^{3+}) is surrounded by six oxygen ions (O^{2-}) attributing a collinear arrangement of A and B-lattices. It gives rise to antiferromagnetic ordering. However, BO_6 octahedra are titled to different degrees based on the diameter of the cation at A-site and show a net magnetic moment [25,26]. Nano-sized LFO exhibits higher specific surface area (S) than its bulk counterpart, due to quantum size effect [21]. It allows various dopants to accommodate in its structure and therefore, the properties can be tuned based on the kind of dopant [27]. Preferential occupation of A-site or B-sites by the doping element can also influence the electrical,

* Corresponding author. Dept of Physics, Thiruvalluvar University, TVUCAS Campus, Thennangur, 604408, Tamil Nadu, India.
** Corresponding author.
E-mail addresses: ibk77@gmail.com (I. Baskaran), maniphysics@gmail.com, mani@tlabs.ac.za (E. Manikandan).

http://dx.doi.org/10.1016/j.jallcom.2017.04.133
0925-8388/

optical and magnetic properties of LFO up to some extent [28]. In the literature, no detailed report is available on the optical and magnetic properties of substitution on B site by Ti ions using co-precipitation method. Hence, Nanocrystalline $LaFe_{1-x}Ti_xO_3$ powders have been prepared for investigating structural, optical and magnetic properties using X-ray diffraction (XRD), energy dispersive X-ray analysis (EDX), transmission electron microscopy (TEM), UV–Visible spectrometer, Fourier transform infrared (FT-IR) spectrometer and vibrating sample magnetometer (VSM) respectively.

2. Experimental procedure

$LaFe_{1-x}Ti_xO_3$ (x = 0.2, 0.4, 0.6 & 0.8) ceramic powders are prepared by Co-precipitation method with the aqueous solutions of $La(NO_3)_2{\cdot}6H_2O$ (99.6% purity, Sigma-Aldrich), Fe $(NO_3)_2{\cdot}9H_2O$ (99.6% purity, Sigma-Aldrich) and Titanium (IV) isopropoxide (99.6% purity, Sigma-Aldrich) mixtures respectively in alkaline medium. The solutions of La $(NO_3)_26H_2O$, Fe $(NO_3)_2{\cdot}9H_2O$ and Titanium (IV) isopropoxide in their stoichiometry (1 g of La $(NO_3)_2{\cdot}6H_2O$ in 50 ml), (0.8 g of Fe $(NO_3)_2{\cdot}9H_2O$ in 50 ml), (0.2 g of titanium (IV) isopropoxide in 50 ml) were dissolved in double distilled water with a constant stirring. The neutralization is carried out by adding the NaOH solution, and the pH is maintained around at 10. The precipitation is formed when the solution continued stirring for 3 h at 80 °C; then the resultant precipitate is cooled to ambient temperature. To remove the additional compounds of sodium and chloride, the precipitate is washed and filtered several times with double distilled water. To remove the water molecules, the precipitate was dried at 100 °C for 12 h. The dried sample was fluffy mass in appearance that is grinded for 2 h using the motor pestle apparatus and the resulting powder was sintered for 3 hrs at 800 °C. After sintering, the sample was once again grinded for 4 h to make uniform particle size. The resultant powder is subjected to XRD (Bruker X-Ray Powder Diffraction Meter, $Cu_{K\alpha}$ λ = 0.15418 nm), SEM/EDAX (SEM with EDX using Carl Zeiss SUPRA-555), JASCO UV–Visible spectrophotometer (V-670 PC), FT-IR spectrophotometer (IR affinity-1, Shimadzu), TEM (TEM: Model Tecnai G20, FEI, USA) andVSM (EV-7 VSM with Max. applied field 15 kO_e) characterization.

3. Results and discussion

3.1. Structural analysis

Fig. 1 depicts the diffraction patterns of $LaFe_{1-x}Ti_xO_3$ (LFTO) nanoparticles. All the reflection planes are in good agreement with the standard JCPDS: 82–1958 of orthorhombic LFO. Few secondary phases (preceded by *) corresponding to La_2TiO_5 are detected for the increased titanium concentrations (x = 0.6–0.8).

The average diameter (D) of the sample is evaluated for the intense peak positions using Scherrer's formula [29]:

$$D = \frac{k\lambda}{\beta \cos\theta} \quad (1)$$

where 'k' is a constant and is approximate equals to 0.9 for a spherical symmetry, 'λ' is X-ray wavelength of $Cu_{K\alpha}$ = 1.5418 Å, 'θ' is diffraction angle and 'β' is full-width half maxima (FWHM).

The established results revealed that the crystallite size is decreasing with the increase of Ti content and found to be varying between ~9 and 26 nm. Respectively, similar kind of trend was

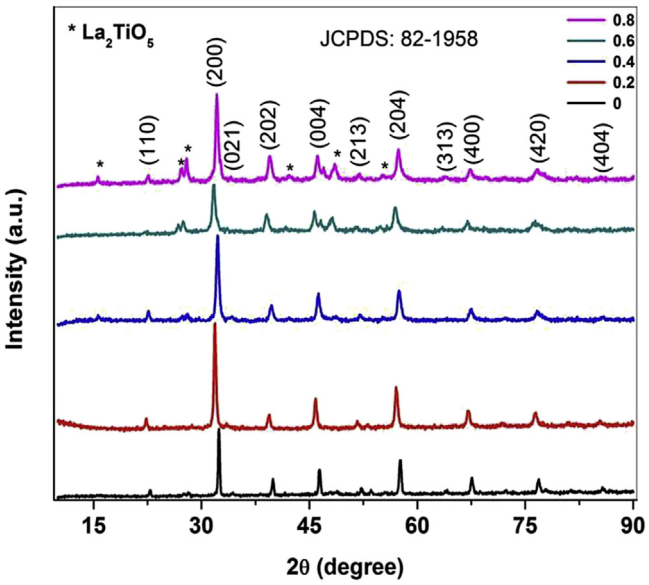

Fig. 1. XRD pattern of $LaFe_{1-x}Ti_xO_3$ (x = 0.2, 0.4, 0.6 & 0.8).

reported [21]. This behaviour is attributed owing to weakening crystal growth or an increase of elastic strain ($\varepsilon = \beta/4\tan\theta$) by Ti-addition. From Table 1, it is evident that ε –value is increasing from 35 × 10^{-4} to 26 × 10^{-3}. The lattice constants (a, b &c) calculated using the formula:

$$\frac{1}{d^2} = \frac{h^2}{a^2} + \frac{k^2}{b^2} + \frac{l^2}{c^2} \quad (2)$$

where 'd' is interplanar spacing distances and hkl are the Miller indices. These are computed using X-powder −12 software. The obtained data is shown in Table 1. A small change of unit cell volume (V = abc) is noticed with titanium addition (Table 1). Iron possible vacancies are Fe^{2+}, Fe^{3+}, and Fe^{+4}. To ensure the charge neutrality and stable orthorhombic structure, Fe^{4+} ions should necessarily be formed in the lattice structure because of +4 valence of titanium. Hence, it removes ferric ions incorporating excess oxygen ions. Lanthanum ions preferentially occupy A-site while iron ions occupy B-site in LFO structure. Upon Ti^{4+} doping, it replaces Fe^{4+} ions. The ionic radii of La^{3+} (0.136 nm), Fe^{4+} (0.058 nm), Ti^{4+} ions (0.061 nm) and O^{2-} (0.155 nm) are responsible for various structural parameters such as tolerance factors (t), lattice constants and X-ray density (D_x) [21]. It is remembered that perovskite

Table 1
Structural parameters of $LaFe_{1-x}Ti_xO_3$ (x = 0.2, 0.4, 0.6 & 0.8).

X	0	0.2	0.4	0.6	0.8
D(nm)	24.6	15.3	11	10	9
FWHM(β)	0.005	0.012	0.019	0.013	0.022
Strain (ε)	0.003	0.007	0.010	0.022	0.026
a(Å)	5.513	5.608	5.534	5.587	5.640
b(Å)	5.473	5.621	5.572	5.520	5.714
c(Å)	7.819	7.911	7.850	7.860	7.931
V $(Å)^3$	235.9	249.3	242.1	242.4	255.6
$D_x(g/cm^3)$	6.833	6.424	6.573	6.521	6.183
S (m^2/g)	35.7	61.1	82.9	92.0	107.8
νcm^{-1}(M - O)	538.1	540.1	551.6	555.5	561.9

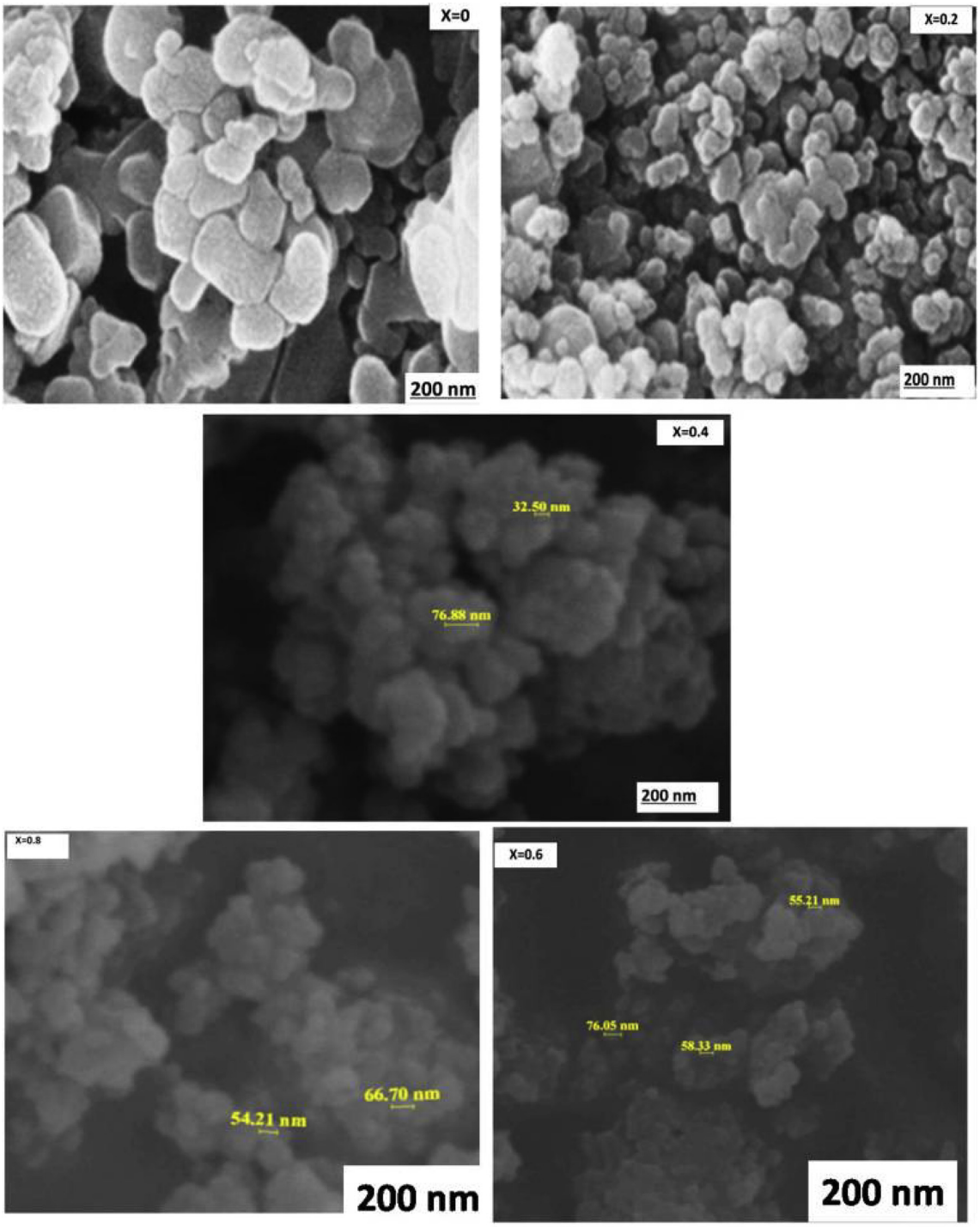

Fig. 2. SEM photographs of $LaFe_{1-x}Ti_xO_3$ (x = 0, 0.2, 0.4, 0.6 & 0.8).

materials perform a stable structure depending upon their tolerance factor (t) and is mathematically given by

$$t = \frac{R_A + R_B}{\sqrt{2}[R_B + R_0]} + \frac{k^2}{b^2} + \frac{l^2}{c^2} \quad (3)$$

where R_A, R_B and R_O are ionic radii of A-site, B-site and oxygen ions respectively. For a stable orthorhombic structure t < 0.96 [30]. In this investigation t-values for $[La^{3+}]_A[Fe^{4+},Ti^{4+}]_BO^{2-}$structure are 0.645 & 0.644(<0.96) with respect to Ti and Fe-ions at B-sites respectively. The high phase purity (absence of secondary phases) at x = 0 & 0.2 shows an increasing trend of lattice constants (Table 1).

Since Ti^{4+} (0.61 Å) ionic radius is greater than that of Fe^{4+} (0.58 Å). On the other hand for x = 0.3–0.8, a unsystematic variation of lattice constants is noticed due to the presence of secondary phases. The X-ray density (D_x) and specific surface area (S) are calculated by following relations [30].

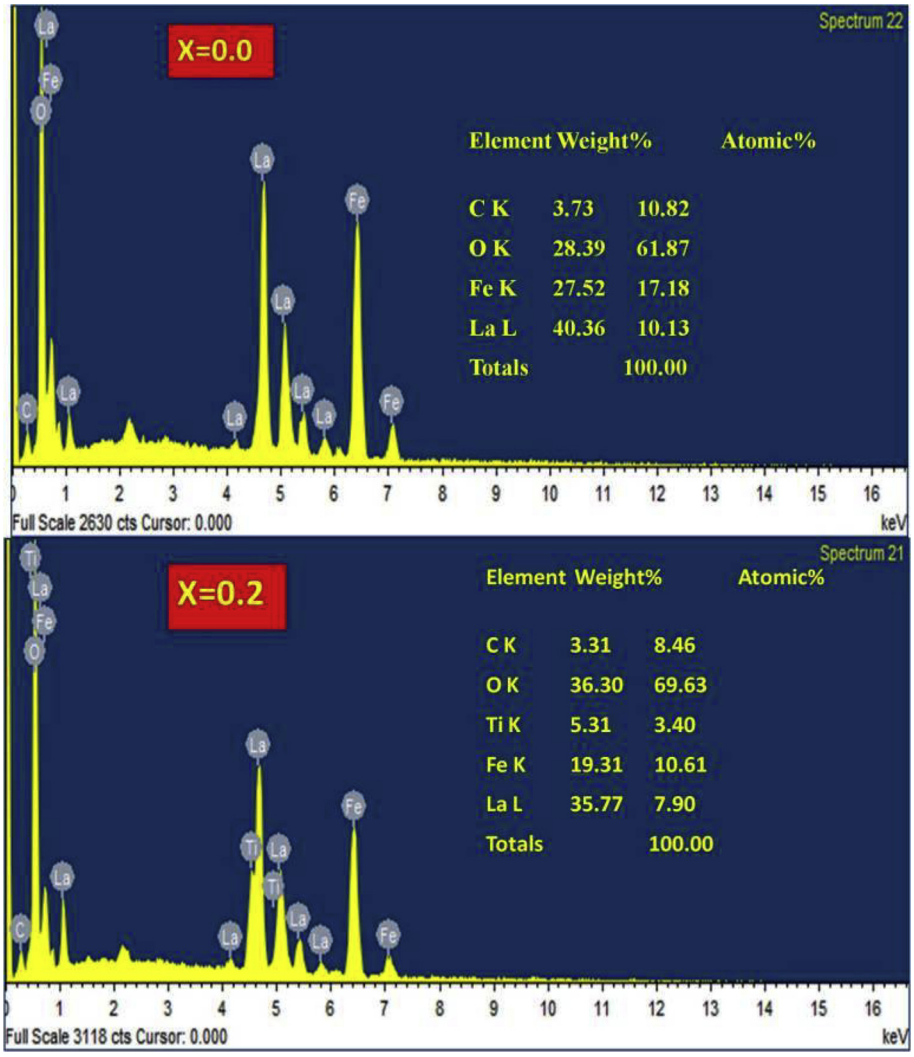

Fig. 3. EDAX spectra of $LaFe_{1-x}Ti_xO_3$(x = 0 & 0.2).

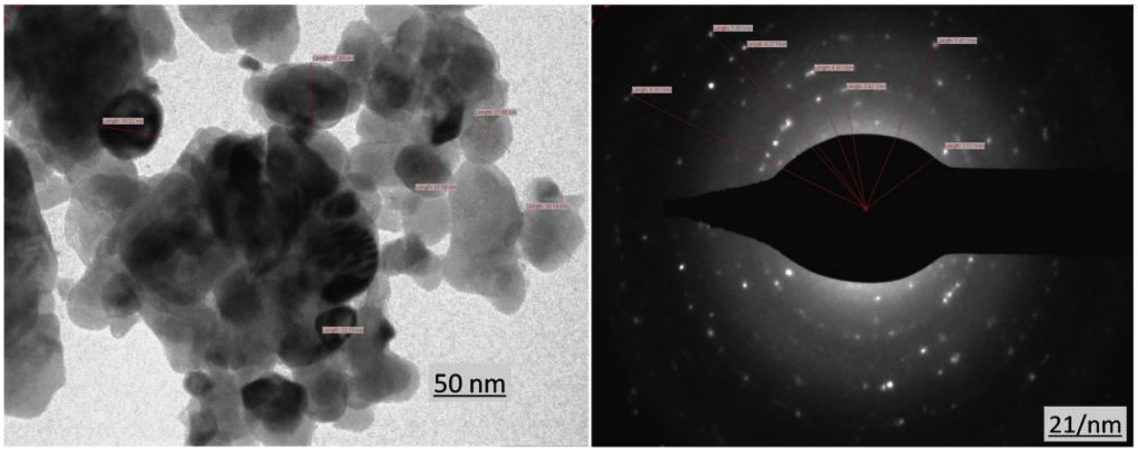

Fig. 4. TEM images of $LaFe_{0.8}Ti_{0.2}O_3$.

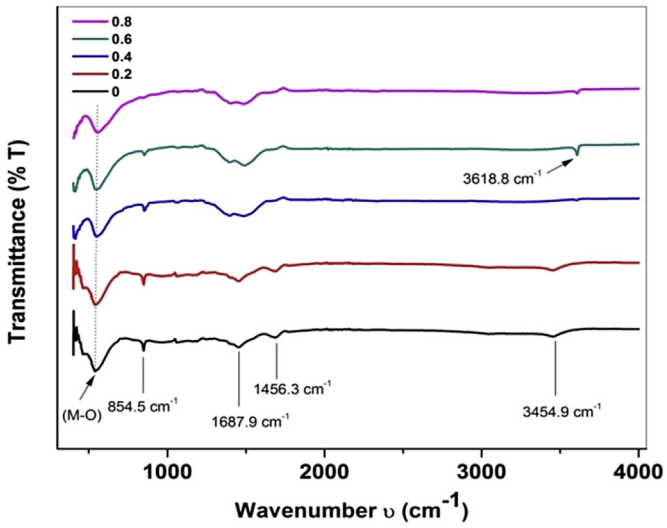

Fig. 5. FTIR spectra of $LaFe_{1-x}Ti_xO_3$ (x = 0, 0.2, 0.4, 0.6 & 0.8).

$$D = \frac{ZM}{Na^3} \tag{4}$$

$$S = \frac{6000}{D^* D_x} \tag{5}$$

where Z (4) is a number of atoms per unit cell, M is the molecular weight and N (6.023×10^{23}) is the Avogadro's number. In respect of the results (Table 1), at increased doping level, D_x is exhibiting unsystematic trend due to presence of secondary phases. The surface area is increasing with rising x-value from 35.7 $m^2\ g^{-1}$ to107.8 $m^2\ g^{-1}$ owing to decrease of crystallite size. This clearly reveals the fact that secondary phases can affect the dimensions, volume of unit cell and density.

3.2. Surface morphology

Surface morphology and elemental analysis of nanoparticles are carried out using scanning electron microscope (SEM) and energy dispersive x-ray analysis (EDAX). In SEM photographs (Fig. 2) show

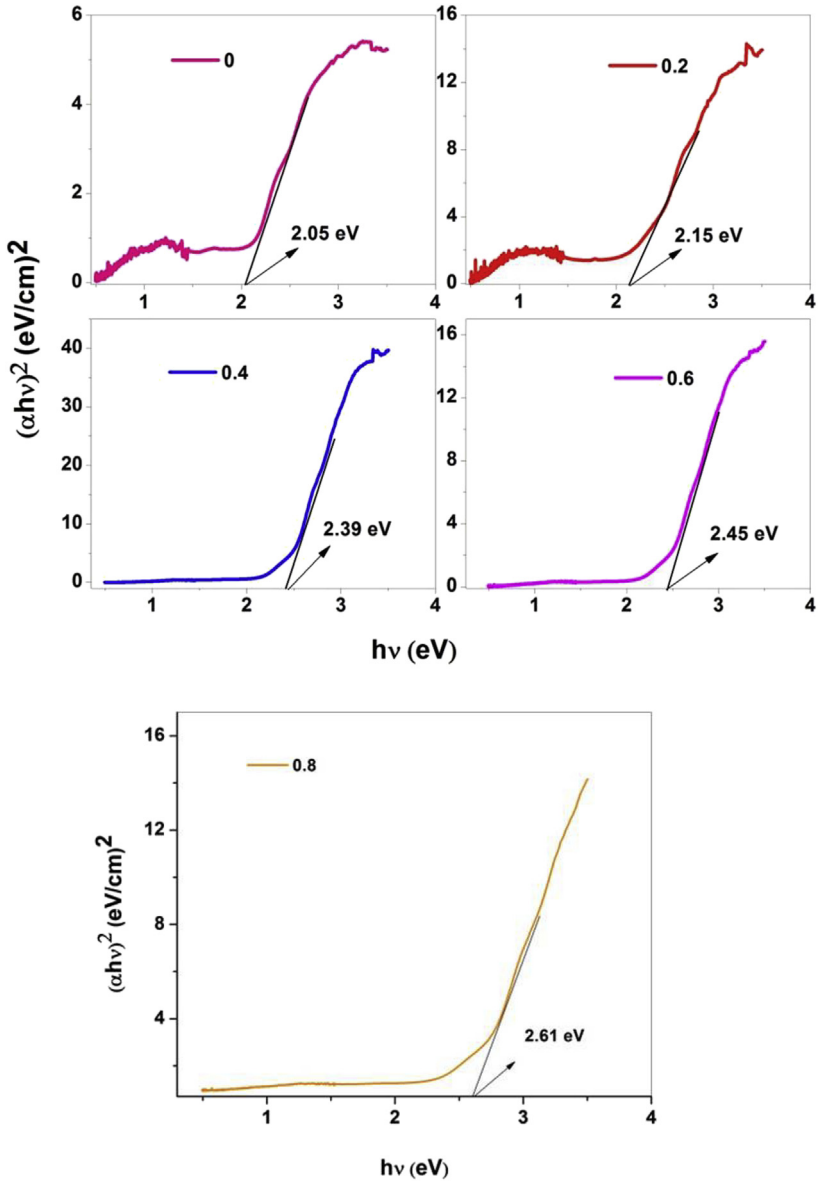

Fig. 6. UV–Visible spectra of $LaFe_{1-x}Ti_xO_3$ (x = 0, 0.2, 0.4, 0.6 & 0.8).

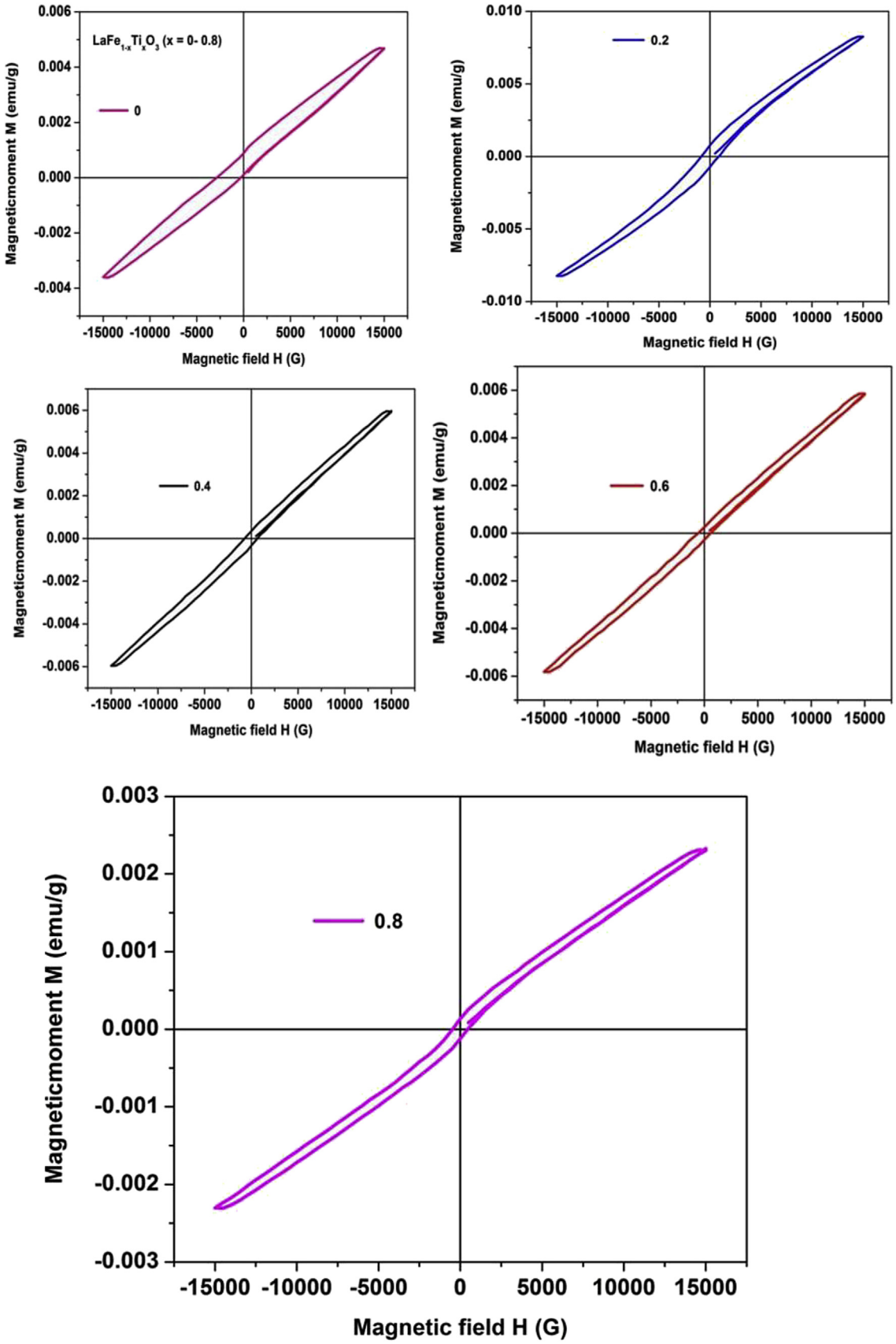

Fig. 7. VSM analysis of $LaFe_{1-x}Ti_xO_3$ (x = 0, 0.2, 0.4, 0.6 & 0.8).

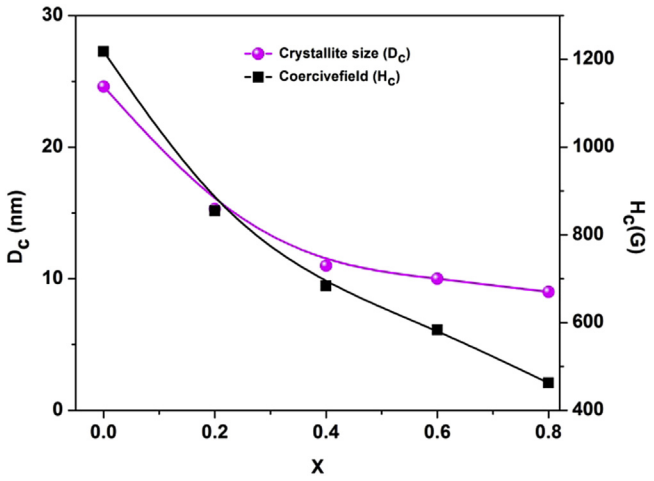

Fig. 8. A graphical representation of dopant *vs.* coercivity and grain size of the nanopowders.

the particle grain size around 39–77 nm grains were detected. This confirms the formation of well nanocrystalline grains during the heat treatment. As far as the shape is concerned, x = 0 & 0.2 showed the flat plate-like grains. However, for the rest compositions almost clustered spherical grains are observed. It is also noticed that the obtained grain sizes (39–77 nm) are approximately identical to the crystallite size (25 - 9 nm) established from diffraction studies. The small enhancement of grain size is due to creeping of grain boundary when the specimen underwent heat treatment. The EDAX spectra show the abundance of elements in the nanopowders and are presented in Fig. 3. The presence of La, Fe, Ti and O elements including their atomic (At%) and weight (Wt%) percentages are reported (inset table of EDAX).

The surface morphology and structure of LFTO is investigated by TEM and selected area electron diffraction (SAED) patterns respectively (Fig. 4). TEM photograph (x = 0.2) shows a small agglomeration among the nanoparticles. This is due to weak magnetic interactions between the particles [17]. The average grain size of 31.4 nm is consistent with the diffraction and SEM results. The SAED pattern shows concentric circular pattern attributing the polycrystalline structure and is very close to the diffraction pattern of XRD (x = 0.2). The SAED pattern lengths are shown in Fig. 4.

3.3. FTIR analysis

Fig. 5 represents the Fourier transform infrared spectra (FT-IR) of $La_{1-x}Ti_xFeO_3$(x = 0, 0.2, 0.4, 0.6 & 0.8) nano-powders. All spectra show broad absorption bands around 540 - 560 cm^{-1}. A small shift is identified for metal-oxide (M - O) towards the higher wave numbers i.e. from 538.1 to 561.9 cm^{-1}. Some more absorption bands are observed at approximately 3618.8 cm^{-1} and 3454.9 cm^{-1}which are designed to the symmetric and asymmetric stretching modes of water molecules [31]. At approximately 1456.3 cm^{-1} and 1687.9 cm^{-1}wave numbers, the bending modes of the O–H bond are observed. A small absorption peak at 854.5 cm^{-1} reveals the presence of metal oxide-bonds which are assigned to the vibrations of Fe–O and O–Fe–O bonds [32].

3.4. UV–Visible absorption spectra

UV–Visible spectroscopy is employed to characterise the optical properties of the LFTO nanoparticles. The direct band gap energy (E_g) was determined by fitting the absorption data to the direct transition as the equation is $\alpha h\nu = A\,(h\nu - E_g)^{1/2}$, where α is the optical absorption coefficient, $h\nu$ is the photon energy, $E_g$is the direct band gap, and A is constant. The extrapolation of the linear parts of the curves toward absorption equal to zero gives E_g for direct transitions (Fig. 6). The estimated direct band gaps of all samples are in the range of 2.05, 2.15, 2.39, 2.45 and 2.61 eV [30,33,38]. The results are in consistent with the reported direct bandgap value of $LaFeO_3$ nanoparticles synthesized by sol–gel auto-combustion method is 2.1 eV [34–36]. These small band gaps of $LaFeO_3$ are interesting for application in photocatalytic [37].

3.5. VSM analysis

The M - H loop behaviour of $LaFe_{1-x}Ti_xO_3$ (x = 0, 0.2, 0.4, 0.6 & 0.8) is studied from vibrating sample magnetometer at room temperature (RT) varying the applied magnetic field (*H*) during the range of 0 to ±15 kOe exhibit (Fig. 7). From hysteresis loop behaviour it is confirmed that the nanopowders exhibit weak ferromagnetic nature having a small M - H loop. This may be due to spin-canted iron moments generated from disordered surface spins [21]. The magnetic parameters are reported in Table 2. It can be seen from the table that magnetisation (M_s), magnetic moment (n_B), remanence (M_r) and squareness are increasing from x = 0–0.2. For further increase of x-value both the parameters are showing a decreasing trend. The attained maximum value of all magnetic parameters other than coercivity (H_c) and anisotropy constant (K_1) is interesting for x = 0.2. High phase purity and an increasing number of uncompensated spins of iron moments, in turn, causes it. Since they can allow the domain wall motion freely; this improves n_B value. Likewise, the presence of secondary phases and high concentration of non-magnetic cations (Ti^{4+}) can hide the domain wall motion. Thus lowers the values of above mentioned magnetic parameters. It is also found that the anisotropy constant and coercivity are decreasing with the increase of non-magnetic cations. This reveals a proportional relationship between H_c and K_1. Normally, coercivity is a crystallite size dependent parameter. At x = 0.8, magnetisation decreases owing to a high AFM spin alignments of Fe^{3+}–O^{2-}–Fe^{3+}& Fe^{4+}-O^{2-}–Fe^{4+} by superexchange interaction. This leads to a reduction of magnetisation. At x = 0.2 the maximum value of magnetisation shows magnetic memory device applications.

Table 2
Magnetic properties of Ti-doped $LaFeO_x$.

X	0	0.2	0.4	0.6	0.8
Coercivity H_c (G)	1217.6	855.0	683.5	583.6	462.5
Magnetisation M_s (emu)	6.49×10^{-3}	8.25×10^{-3}	5.97×10^{-3}	5.83×10^{-3}	2.32×10^{-3}
Retentivity M_r (emu)	542.9×10^{-6}	747.2×10^{-6}	339.6×10^{-6}	264.5×10^{-6}	127.7×10^{-6}
Squareness (M_r/M_s)	0.084	0.091	0.057	0.045	0.055
Magnetic moment (n_B)	2.82×10^{-4}	3.56×10^{-4}	2.56×10^{-4}	2.48×10^{-4}	9.82×10^{-4}
Anisotropy constant (K)	8.23	7.35	4.25	3.54	1.12

From Fig. 8, it is obvious that the coercivity is decreasing with the increase of x-value due to a decrease in crystallite size (D_c). Several researchers have reported the inverse relation of H_c and D_c based on domain theory [39]. However, in this investigation, a proportional relation is established. According to Stoner-Wohlfarth model [39], for a weak ferromagnetic single domain particle, H_c decreases as the particle size decreases due to a decrease of magnetic moment and anisotropy constant [40–43].

4. Conclusion

Nanoparticles of $LaFe_{1-x}Ti_xO_3$ ($x = 0, 0.2, 0.4, 0.6, 0.8$) have been prepared by Co-precipitation method. The average crystallite size (D_c) is varying between 9 nm and 24.6 nm. The morphology is analyzed using scanning electron microscope and transmission electron microscope. The E_g values are increasing with dopant from 2.05 eV to 2.61 eV. The weak ferromagnetic behaviour is observed from hysteresis loop behaviour. Coercivity (H_c) and anisotropy constants (K_1) are eventually decreasing with 'x' value. At $x = 0.2$ the maximum value of magnetisation shows magnetic memory device applications.

Acknowledgment

We gratefully acknowledges support from Arignar Govt Arts College- Cheyyar (TNTVU-2016/15), and thanks for the characterization facility VIT University, Vellore, Tamil Nadu, India. We also express our thanks to IIT Chennai and IIT Bombay for recording VSM and TEM analysis of the samples.

References

[1] E. Hema, A. Manikandan, P. Karthika, M. Durka, S. Arul Antony, B.R. Venkatraman, A novel synthesis of Zn^{2+}-doped $CoFe_2O_4$ spinel nanoparticles: structural, morphological, opto-magnetic and catalytic properties, J. Supercond. Nov. Magn. 28 (8) (2015) 2539–2552.
[2] K. Thanigai Arul, E. Manikandan, R. Ladchumananandasivam, M. Maaza, Novel polyvinyl alcohol polymer based nanostructure with ferrites co-doped with nickel and cobalt ions for magneto-sensor application, Polym. Int. 65 (2016) 1482–1485.
[3] A. Manikandan, S. Arul Antony, R. Sridhar, Seeram Ramakrishna, M. Bououdina, A simple combustion synthesis and optical studies of magnetic $Zn_{1-x}Ni_xFe_2O_4$ nanostructures for photoelectron chemical applications, J. Nanosci. Nanotechnol. 15 (2015) 4948–4960.
[4] J. Kennedy, J. Leveneur, G.V.M. Williams, D.R.G. Mitchell, A. Markwitz, Fabrication of surface magnetic nanoclusters using low energy ion implantation and electron beam annealing, Nanotechnology 22 (2011) 115602.
[5] J. Kennedy, et al., Intrinsic magnetic order and inhomogeneous transport in Gd-implanted zinc oxide, Phys. Rev. B 88 (21) (2013) 214423.
[6] E. Manikandan, L. Krishnakumar, G. Kavitha, G. Mani, Effective ammonia detection using n-ZnO/p-NiO heterostructured nanofibers, IEEE Sens. J. 16 (2015) 2477–2483.
[7] A.H. Shah, M.B. Ahamed, E. Manikandan, R. Chandramohan, M. Iydroose, Magnetic, optical and structural studies on Ag doped ZnO nanoparticles, J Mater. Sci. Mater. Electron. 24 (2013) 2302–2308.
[8] J. Leveneur, J. Kennedy, G.V.M. Williams, J. Metson, A. Markwitz, Large room temperature magnetoresistance in ion beam synthesized surface Fe nanoclusters on SiO2, Appl. Phys. Lett. 98 (2011) 053111.
[9] K. Chinnaraj, A. Manikandan, P. Ramu, S. Arul Antony, P. Neeraja, Comparative study of microwave and sol-gel assisted combustion methods of Fe_3O_4 nanostructures: structural, morphological, optical, magnetic and catalytic properties, J. Supercond. Nov. Magn. 28 (2015) 179–190.
[10] V. Mary Teresita, A. Manikandan, B. Avila Josephine, S. Sujatha, S. Arul Antony, Electro-magnetic properties and humidity sensing studies of magnetically recoverable $LaMg_xFe_{1-x}O_{3-\delta}$ perovskites nano-photocatalysts by sol-gel route, J. Supercond. Nov. Magn. 29 (2016) 1691–1701.
[11] S. Rajmohan, V. Jeseentharani, A. Manikandan, John Pragasam, Co-precipitation synthesis method, characterizations and humidity sensing applications of perovskite-type mixed oxide $La_{1-x}Co_xVO_{3-\delta}$ nanocomposites, Nanosci. Nanotechnol. Lett. 8 (2016) 393–398.
[12] B. Avila Josephine, A. Manikandan, V. Mary Teresita, S. Arul Antony, Fundamental study of $LaMg_xCr_{1-x}O_{3-\delta}$ perovskites nano-photocatalysts: sol-gel synthesis, characterization and humidity sensing, Korean J. Chem. Eng. 33 (2016) 1590–1598.
[13] S. Khamlich, E. Manikandan, B.D. Ngom, J. Sithole, O. Nemraoui, I. Zorkani, Synthesis, characterization, and growth mechanism of α-Cr_2O_3 monodispersed particles, J. Phys. Chem. Solids 72 (2011) 714–718.
[14] A. Manikandan, M. Durka, S. Arul Antony, Magnetically recyclable spinel $Mn_xZn_{1-x}Fe_2O_4$; ($0 \le x \le 0.5$) nano-photocatalysts, Adv. Sci. Eng. Med. 7 (2015) 33–46.
[15] M.F. Valan, A. Manikandan, S. Arul Antony, Microwave combustion synthesis and characterization studies of magnetic $Zn_{1-x}Cd_xFe_2O_4$ ($0 \le x \le 0.5$) nanoparticles, J. Nanosci. Nanotechnol. 15 (2015) 4543–4551.
[16] E.A. Tugova, et al., Phase diagram of the $LaFeO_3$-$LaSrFeO_4$ system, Glass Phys. Chem. 32 (2006) 674–676.
[17] S. Petrović, et al., $LaMO_3$ (M= Mg, Ti, Fe) perovskite type oxides: preparation, characterization and catalytic properties in methane deep oxidation, Appl. Catal. B Environ. 79 (2008) 186–198.
[18] Saumitra N. Tijare, et al., Photocatalytic hydrogen generation through water splitting on nano-crystalline $LaFeO_3$ perovskite, Int. J. Hydrogen Energy 37 (2012) 10451–10456.
[19] Zhi-Xian Wei, et al., Preparation and catalytic activities of $LaFeO_3$ and Fe_2O_3 for HMX thermal decomposition, J. Hazard. Mater. 165 (2009) 1056–1061.
[20] Jérémy Faye, et al., Influence of lanthanum stoichiometry in La1− xFeO3−δ perovskites on their structure and catalytic performance in CH4 total oxidation, Appl. Catal. B Environ. 126 (2012) 134–143.
[21] Sumalin Phokha, et al., Polymerized complex synthesis and effect of Ti-Dopant on magnetic properties of $LaFeO_3$ nanoparticles, J. Nanosci. Nanotechnol. 15 (2015) 9171–9177.
[22] P. Jain, S. Srivastava, Investigation of structural, magnetic and electrical properties of pure $LaFeO_3$ synthesized through solution combustion technique, Dig. J. Nanomater. Biostruct. 10 (1) (2015) 141–147.
[23] D. Treves, Studies on orthoferrites at the Weizmann institute of science, J. Appl. Phys. 36 (3) (1965) 1033–1039.
[24] Yuri S. Didosyan, et al., Magneto-optical rotational speed sensor, Sens. Actuators A Phys. 106.1 (2003) 168–171.
[25] Sanjay Mathur, et al., Molecule derived synthesis of nanocrystalline YFeO3 and investigations on its weak ferromagnetic behavior, Chem. Mater. 16 (10) (2004) 1906–1913.
[26] Sanjay Mathur, et al., Nanocrystalline orthoferrite GdFeO3 from a novel heterobimetallic precursor, Adv. Mater. 14.19 (2002) 1405–1409.
[27] Preet Shikha, Tejwant Singh Kang, B.S. Randhawa, Effect of different synthetic routes on the structural, morphological and magnetic properties of Ce doped LaFeO 3 nanoparticles, J. Alloys Compd. 625 (2015) 336–345.
[28] Luís G. Tejuca, J.L.G. Fierro (Eds.), Properties and Applications of Perovskite-type Oxides, CRC Press, 2000.
[29] Mohamed H. Mahmoud, et al., Synthesis of highly ordered 30nm NiFe 2 O 4 particles by the microwave-combustion method, J. Magn. Magn. Mater. 369 (2014) 55–61.
[30] Manh-Huong Phan, Seong-Cho Yu, Review of the magnetocaloric effect in manganite materials, J. Magn. Magn. Mater. 308 (2) (2007) 325–340.
[31] Nguyen Thi Thuy, Dang Le Minh, Size effect on the structural and magnetic properties of nanosized perovskite LaFeO3 prepared by different methods, Adv. Mater. Sci. Eng. 2012 (2012).
[32] Yutana Janbutrach, Sitchai Hunpratub, Ekaphan Swatsitang, Ferromagnetism and optical properties of La 1− x Al x FeO 3 nanopowders, Nanoscale Res. Lett. 9 (1) (2014) 498.
[33] Zhongqin Yang, et al., Influence of parameters U and J in the LSDA+U method on electronic structure of the perovskites La M O 3 (M= C r, M n, F e, C o, N i), Phys. Rev. B 60 (23) (1999) 15674.
[34] Saad, A. Abdullah, et al., Structural, optical and magnetic properties of perovskite $(La_{1-x}Sr_x)(Fe_{1-x}Ni_x)O_3$, (x= 0.0, 0.1 & 0. 2) nanoparticles, Electron. Mater. Lett. 9 (1) (2013) 77–81.
[35] J. Kennedy, et al., Controlling preferred orientation and electrical conductivity of zinc oxide thin films by post growth annealing treatment, Appl. Surf. Sci. 367 (2016) 52–58.
[36] F.T. Thema, E. Manikandan, A. Gurib-Fakim, M. Maaza, Single phase Bunsenite NiO nanoparticles green synthesis by Agathosma betulina natural extract, J. Alloys Compd. 657 (2016) 655–661.
[37] R. Dhinesh Kumar, R. Thangappan, R. Jayavel, Synthesis and characterization of $LaFeO_3/TiO_2$ nanocomposites for visible light photocatalytic activity, J. Phys. Chem. Solids 101 (2017) 25–33.
[38] M.A. Rafiq, M.A. Khan, M. Asghar, S.Z. Ilyas, I. Shakir, M. Shahid, M.F. Warsi, Ceram. Int. 46 (2015), http://dx.doi.org/10.1016/j.ceramint.2015.04.141.
[39] Edmund C. Stoner, E.P. Wohlfarth, A mechanism of magnetic hysteresis in heterogeneous alloys, Philos. Trans. R. Soc. Lond. A Math. Phys. Eng. Sci. 240 (826) (1948) 599–642.
[40] G. Padmapriya, A. Manikandan, V. Krishnasamy, Saravana Kumar Jaganathan, S. Arul Antony, Spinel $Ni_xZn_{1-x}Fe_2O_4$ ($0.0 \le x \le 1.0$) nano-photocatalysts: synthesis, characterization and photocatalytic degradation of methylene blue dye, J. Mol. Struct. 1119 (2016) 39–47.
[41] A.H. Shah, E. Manikandan, M.B. Ahamed, D.A. Mir, S.A. Mir, Antibacterial and Blue shift investigations in sol–gel synthesized $Cr_xZn_{1-x}O$ nanostructures, J. Lumin. 145 (2014) 944–950.
[42] C. Barathiraja, A. Manikandan, A.M. Uduman Mohideen, S. Jayasree, S. Arul Antony, Magnetically recyclable spinel $Mn_xNi_{1-x}Fe_2O_4$ ($x = 0.0–0.5$) nano-photocatalysts: structural, morphological and opto-magnetic properties, J. Supercond. Nov. Magn. 29 (2016) 477–486.
[43] A. Diallo, T.B. Doyle, B.M. Mothudi, E. Manikandan, V. Rajendran, M. Maaza, Magnetic behavior of biosynthesized Co_3O_4 nanoparticles, J. Magn. Magn. Mater. 424 (2017) 251–255.